

Article

Multi-Parameter Fuzzy-Based Neural Network Sensorless PMSM Iterative Learning Control Algorithm for Vibration Suppression of Ship Rim-Driven Thruster

Zhi Yang^{1,2}, Xinping Yan^{1,2,3,*}, Wu Ouyang^{1,2,3,*}, Hongfen Bai^{1,4} and Jinhua Xiao¹ 

¹ School of Transportation and Logistics Engineering, Wuhan University of Technology, Wuhan 430063, China; zhiyang@whut.edu.cn (Z.Y.); xpyan@whut.edu.cn (X.Y.); hfbai@shmtu.edu.cn (H.B.); xiaojinh@whut.edu.cn (J.X.)

² Reliability Engineering Institute, National Engineering Research Center for Water Transport Safety, Wuhan 430063, China

³ State Key Laboratory of Maritime Technology and Safety, Wuhan University of Technology, Wuhan 430063, China

⁴ Key Laboratory of Transport Industry of Marine Technology and Control Engineering, Shanghai Maritime University, Shanghai 201306, China

* Correspondence: ouyangw@whut.edu.cn

Abstract: Aiming to reduce motor speed estimation and torque vibration present in the permanent magnet synchronous motors (PMSMs) of rim-driven thrusters (RDTs), a position-sensorless control algorithm using an adaptive second-order sliding mode observer (SMO) based on the super-twisting algorithm (STA) is proposed. In which the sliding mode coefficients can be adaptively tuned. Similarly, an iterative learning control (ILC) algorithm is presented to enhance the robustness of the velocity adjustment loop. By continuously learning and adjusting the difference between the actual speed and given speed of RDT motor through ILC algorithm, online compensation for the q-axis given current of RDT motor is achieved, thereby suppressing periodic speed fluctuations during motor running. Fuzzy neural network (FNN) training can be used to optimize the STA-SMO and ILC parameters of RDT control system, while improving speed tracking accuracy. Finally, simulation and experimental verifications have been conducted on the vector control system based on the conventional PI-STA and modified ILC-STA. The results show that the modified algorithm can effectively suppress the estimated speed and torque ripple of RDT motor, which greatly improves the speed tracking accuracy.

Keywords: rim-driven thruster (RDT); permanent magnet synchronous motor (PMSM); position-sensorless control; super-twisting algorithm (STA); iterative learning control (ILC); fuzzy neural network (FNN)



Citation: Yang, Z.; Yan, X.; Ouyang, W.; Bai, H.; Xiao, J. Multi-Parameter Fuzzy-Based Neural Network Sensorless PMSM Iterative Learning Control Algorithm for Vibration Suppression of Ship Rim-Driven Thruster. *J. Mar. Sci. Eng.* **2024**, *12*, 396. <https://doi.org/10.3390/jmse12030396>

Academic Editor: Mohamed Benbouzid

Received: 29 January 2024

Revised: 17 February 2024

Accepted: 22 February 2024

Published: 25 February 2024



Copyright: © 2024 by the authors. Licensee MDPI, Basel, Switzerland. This article is an open access article distributed under the terms and conditions of the Creative Commons Attribution (CC BY) license (<https://creativecommons.org/licenses/by/4.0/>).

1. Introduction

Electric propulsion systems have undergone significant development in recent years due to their advanced control efficiency and performance. The rim-driven thruster (RDT) is a new type of low-carbon emission electric thruster, which integrates the propeller blade and the motor together by embedding the motor into the duct. This new type of electric thruster can eliminate the need for shaft transmission, mechanical seals, and oil circuit systems in traditional ship propulsion systems. It can save space for cabins on ships, improve motor efficiency and hydrodynamic efficiency, and reduce system installation complexity and manufacturing costs [1]. For the development of this new type of electric thruster, the selection of the propulsion motor RDT and its control algorithm are the key technologies.

At present, alternating current (AC) induction motors, brushless direct current (BLDC) motors, permanent magnet synchronous motors (PMSM), and high-temperature superconducting motors are included for the selection of RDT motors. Considering the work

efficiency, manufacturing costs and processes performance of RDT, PMSM is currently considered the best choice for RDT propulsion motor. In order to accomplish the vector control of PMSM, it is necessary to obtain accurate rotor position information using position sensors. However, traditional mechanical position sensors (i.e., photoelectric encoders, resolvers, etc.) need to be mounted on the transmission shaft, which does not exist in RDT. They also have problems regarding large size, high costs, and low reliability, especially in specific engineering applications. RDT has a compact structure without the transmission shaft that can work in a harsh underwater environment, see Figure 1. Therefore, it is of great significance to develop anti-chattering position-sensorless control algorithms for RDT drive motors to realize high-performance control [2,3]. The PMSM position-sensorless control algorithms mainly include direct calculation methods, back-EMF integration methods, model reference adaptive methods, and various observer methods [4–8].

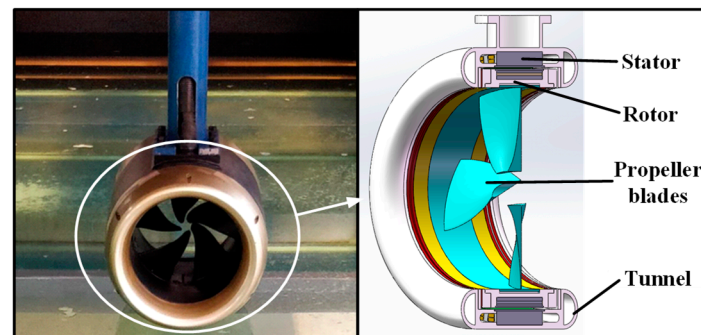


Figure 1. Physical diagram and geometric structure of an RDT.

Of these, the sliding mode observer (SMO) can reduce the dependence on motor parameters with advantages of having a fast response speed, strong robustness, and simple structure. Therefore, it is widely used in the position-sensorless control of PMSM [9]. The chattering will occur in the control system when using the SMO algorithm due to the switching of the sliding mode surface [10]. Especially in the vector control of PMSM at low speeds, it causes relatively large torque ripples. Therefore, it is necessary to eliminate chattering while maintaining control accuracy when using the SMO algorithm. The current research mainly focuses on the comprehensive improvement of switching function, sliding mode gain, estimation accuracy, etc. [11–14]. The first-order SMO always has chattering problems, which have a negative impact on the stability of the system. The second-order SMO can effectively eliminate chattering while maintaining the system robustness [15,16] and is well received by many scholars.

Due to the influences of motor design, inverter nonlinearities, and current detection errors, the PMSM control system suffers from torque vibration with current harmonics, which also reduces speed control accuracy. Usually, the vibration of motor torque is suppressed by optimizing motor design or improving the motor control strategy. However, it is difficult to modify the design after completing the original motor design [17]. With the development of control theory, many improved control strategies have been proposed to reduce torque vibration suppression, such as harmonic voltage injection, proportional-integral quasi-resonant compensator, and dead-zone feedforward compensation [18,19]. Iterative learning control (ILC) is an approach to improve the performance of a system that executes repetitively and periodically over a fixed time interval by learning from previous executions (trials, iterations, and passes) [20]. It does not rely on the mathematical model of systems and can be used in PMSM control to effectively improve tracking performance and compensate the control signal through continuous learning [21].

This paper presents a RDT position-sensorless control algorithm using an adaptive second-order SMO based on the super-twisting algorithm (STA). An adaptive algorithm is used to tune the sliding mode coefficients. Furthermore, a torque ripple suppression method based on ILC algorithm is proposed. A closed-loop PI-ILC algorithm with a forgetting factor is introduced to compensate for the q -axis given current through iterative

learning, thereby reducing the real-time speed error. Considering the error and error rate of motor speed as input, and fuzzy neural network (FNN) training is used to optimize the ILC and STA-SMO parameters to improve the accuracy and stability of the control system. The proposed control algorithm can suppress the motor speed torque vibration and improve the speed tracking accuracy. The main innovations of this paper are as follows:

- (1) A RDT control strategy using an adaptive second-order SMO based on the STA is designed.
- (2) To reduce the torque ripple suppression of RDT motor, a closed-loop PI-ILC algorithm is introduced to compensate the speed real-time error to the q -axis given current.
- (3) FNN training is used to optimize the ILC and STA-SMO parameters to improve the accuracy and stability of the current loop.

The rest of this paper is organized as follows: Section 2 introduces the materials and methods of RDT motor model and proposed control algorithm. Section 3 introduces the application of multi-parameter FNN for parameter tuning. Section 4 introduces the simulation results and discussions of a RDT motor sensorless control model on MATLAB R2017b/Simulink environment. Section 5 introduces the experimental results and the discussions of a RDT motor sensorless control system on experimental setup. The final section presents the conclusions and subsequent ideas of the topic covered in this paper.

2. Materials and Methods

The mathematic current model of the RDT motor in the $\alpha\beta$ -axis reference system can be expressed as:

$$\begin{cases} \frac{di_\alpha}{dt} = -\frac{R_s}{L_s}i_\alpha + \frac{1}{L_s}u_\alpha - \frac{1}{L_s}e_\alpha \\ \frac{di_\beta}{dt} = -\frac{R_s}{L_s}i_\beta + \frac{1}{L_s}u_\beta - \frac{1}{L_s}e_\beta \end{cases} \quad (1)$$

where i_α and i_β and u_α and u_β represent the current and voltage in $\alpha\beta$ -axis reference system, respectively. L_s and R_s represent the inductance and resistance of stator winding.

e_α and e_β represent the back EMFs in $\alpha\beta$ -axis reference system and can be expressed as:

$$\begin{cases} e_\alpha = -\omega\psi_f \sin \theta \\ e_\beta = \omega\psi_f \cos \theta \end{cases} \quad (2)$$

where ψ_f is the flux linkages and ω and θ represent the rotor speed and position of the RDT motor.

2.1. Adaptive STA-SMO

The super-twisting algorithm (STA) was first proposed by A. Levant to effectively eliminate the chattering problem of first-order SMO. The basic form of STA with perturbation was designed as [22]:

$$\begin{cases} \frac{dx_1}{dt} = -k_1|\tilde{x}_1|^{1/2}\text{sgn}(\tilde{x}_1) + x_2 + z_1(x_1, t) \\ \frac{dx_2}{dt} = -k_2\text{sgn}(\tilde{x}_1) + z_2(x_2, t) \end{cases} \quad (3)$$

where x_1 , x_2 , and \tilde{x}_1 are the state variables, error between estimated values, and actual values of the state variables. k_1 and k_2 are designed to be the sliding-mode coefficients of STA. z_1 and z_2 are perturbation terms of system.

The stable conditions of STA have been proved in [23,24], demonstrating that the perturbation terms should be globally bounded by:

$$\begin{cases} |z_1| \leq \delta_1|x_1|^{1/2} \\ |z_2| = 0 \end{cases} \quad (4)$$

And the sliding mode coefficients k_1 and k_2 should satisfy (5) to stabilize the system:

$$\begin{cases} k_1 > 2\delta_1 \\ k_2 > k_1 \frac{5\delta_1 k_1 + 4\delta_1^2}{2k_1 - 4\delta_1} \end{cases} \quad (5)$$

where $\delta_1 > 0$ and is a normal number.

In order to obtain the estimated value of the back EMF, the stator currents of RDT motor are estimated using STA based second-order SMO [15,16]:

$$\begin{cases} \frac{d\hat{i}_\alpha}{dt} = -\frac{R_s}{L_s}\hat{i}_\alpha + \frac{1}{L_s}u_\alpha + \frac{1}{L_s}k_1|\tilde{i}_\alpha|^{1/2}\text{sgn}(\tilde{i}_\alpha) + \frac{1}{L_s}\int k_2\text{sgn}(\tilde{i}_\alpha)dt \\ \frac{d\hat{i}_\beta}{dt} = -\frac{R_s}{L_s}\hat{i}_\beta + \frac{1}{L_s}u_\beta + \frac{1}{L_s}k_1|\tilde{i}_\beta|^{1/2}\text{sgn}(\tilde{i}_\beta) + \frac{1}{L_s}\int k_2\text{sgn}(\tilde{i}_\beta)dt \end{cases} \quad (6)$$

in which \hat{i}_α and \hat{i}_β denote the estimated values of i_α and i_β . By comparing Equation (3) with Equation (6), it can be concluded that perturbation terms z_1 and z_2 are designed through:

$$\begin{cases} z_1(\hat{i}_\alpha, t) = -\frac{R_s}{L_s}\hat{i}_\alpha + \frac{1}{L_s}u_\alpha \\ z_1(\hat{i}_\beta, t) = -\frac{R_s}{L_s}\hat{i}_\beta + \frac{1}{L_s}u_\beta, z_2 = 0 \end{cases} \quad (7)$$

By substituting Equation (7) into Equation (4), we obtain:

$$\begin{cases} -\frac{R_s}{L_s}\hat{i}_\alpha + \frac{1}{L}u_\alpha - \delta_1|\hat{i}_\alpha|^{1/2} \leq 0 \\ -\frac{R_s}{L_s}\hat{i}_\beta + \frac{1}{L}u_\beta - \delta_1|\hat{i}_\beta|^{1/2} \leq 0 \end{cases} \quad (8)$$

For a sufficiently large δ_1 , the validity of the above inequality can be met. The state equations of currents errors in $\alpha\beta$ -axis reference system can be derived by subtracting Equation (1) from Equation (6):

$$\begin{cases} \frac{d\tilde{i}_\alpha}{dt} = -\frac{R_s}{L_s}\tilde{i}_\alpha + \frac{1}{L_s}(k_1|\tilde{i}_\alpha|^{1/2}\text{sgn}(\tilde{i}_\alpha) + \int k_2\text{sgn}(\tilde{i}_\alpha)dt + e_\alpha) \\ \frac{d\tilde{i}_\beta}{dt} = -\frac{R_s}{L_s}\tilde{i}_\beta + \frac{1}{L_s}(k_1|\tilde{i}_\beta|^{1/2}\text{sgn}(\tilde{i}_\beta) + \int k_2\text{sgn}(\tilde{i}_\beta)dt + e_\beta) \end{cases} \quad (9)$$

When the system reaches the sliding surface and the estimated error is close to 0 ($\tilde{i}_\alpha = 0, \tilde{i}_\beta = 0$). The equivalent back-EMFs e_α and e_β can be obtained by the equivalent control method, it can be concluded that:

$$\begin{cases} e_\alpha = -k_1|\tilde{i}_\alpha|^{1/2}\text{sgn}(\tilde{i}_\alpha) - \int k_2\text{sgn}(\tilde{i}_\alpha)dt \\ e_\beta = -k_1|\tilde{i}_\beta|^{1/2}\text{sgn}(\tilde{i}_\beta) - \int k_2\text{sgn}(\tilde{i}_\beta)dt \end{cases} \quad (10)$$

where k_1 and k_2 are the sliding mode coefficients. It is difficult to determine the actual values of k_1 and k_2 in practice. And different sets of k_1 and k_2 will influence the stability conditions of STA-SMO. Therefore, it is crucial to adaptively adjust the sliding mode coefficients. The adaptive algorithm is given as:

$$\begin{cases} k_1 = \sigma_1\omega \\ k_2 = \sigma_2\omega^2 \end{cases} \quad (11)$$

in which σ_1 and σ_2 are adaptive coefficients. The stability of the adaptive algorithm has been proved in [16].

The rotor position estimation method based on the arctangent function will directly introduce the sliding mode chattering into the division operation, resulting in significant estimation errors. Therefore, the PLL structure is used to extract the rotor position information of the RDT motor. It can suppress chattering and maintain good control performance. The structure block diagram of the adaptive STA-SMO is shown in Figure 2.

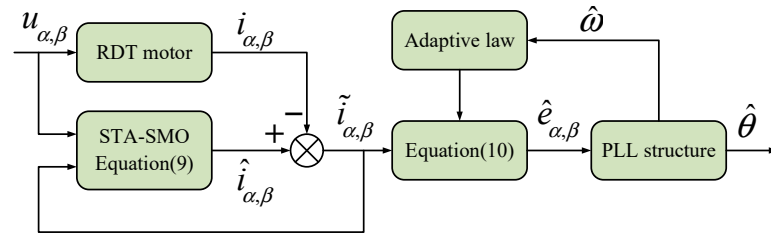


Figure 2. Structure block diagram of the adaptive STA-SMO.

2.2. Design of ILC Algorithm

By analyzing the previous control data, ILC can find appropriate control input through real-time online iteration, theoretically obtaining accurate tracking trajectories.

Traditional PI control achieves satisfactory results by selecting appropriate proportional and integral parameters but struggles to meet high-precision control requirements. By introducing the ILC algorithm to form an ILC controller, the q -axis given current of motor can be obtained with ILC controller and traditional PI controller.

The type of PI-ILC algorithm is adopted to acquire the learning law [19]:

$$i_{q,k+1}^*(t) = (1 - \alpha)i_{q,k}^*(t) + \eta e_{k+1}(t) + \xi \int e_{k+1}(t)dt \tag{12}$$

where $i_{q,k+1}^*(t)$ is the reference signal of the current cycle's q -axis current; $i_{q,k}^*(t)$ is the reference signal of the q -axis current in the previous cycle called the "learning experience"; $e_{k+1}(t)$ is the current cycle speed deviation signal, which is mainly used to compensate for the "learning experience" loss caused by the forgetting factor; and η and ξ are the closed-loop learning coefficients. Formula (12) in the z -domain is shown as:

$$i_{q,k+1}^*(z) = (1 - \alpha)i_{q,k}^*(z) + \eta e_{k+1}(z) + \xi \frac{z}{z - 1} e_{k+1}(z) \tag{13}$$

The iterative process can be regarded as a delay link, which is shown as:

$$z^{-N}i_{q,k+1}^*(z) = i_{q,k}^*(z) \tag{14}$$

in the above equation, $N = f_{sample} / f_{signal}$, f_{sample} represents the sampling frequency of the digital control system, while f_{signal} is the system signal frequency.

When N takes a value of 1, the z -domain transfer function of the equation is shown as:

$$G(z) = \frac{i_{q,k+1}^*(z)}{e_{k+1}(z)} = \frac{(\eta + \xi)z^2 - \eta}{z^2 - (2 - \alpha)z + (1 - \alpha)} \tag{15}$$

The structure block diagram of ILC process and closed-loop PI-ILC are shown in Figures 3 and 4.

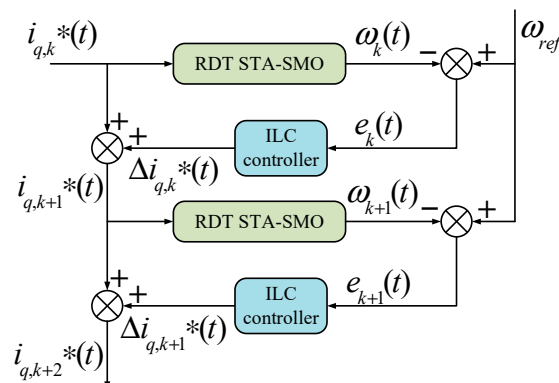


Figure 3. Structure block diagram of the ILC process.

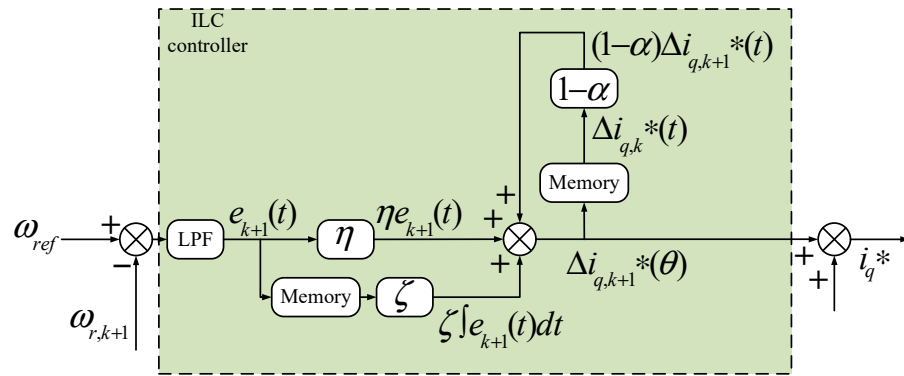


Figure 4. Structure block diagram of the closed-loop PI-ILC.

The design of the ILC controller should not only ensure its stability but also ensure that the iterative algorithm converges to its true value. The convergence conditions of the PI type iterative algorithm are determined as follows.

Combining Formulas (12) and (15) through $e_{k+1} = \omega_{ref} - \omega_{r,k+1}$, it can be seen that:

$$e_{k+1} = \omega_{ref} - \frac{n_p k_t}{J} \left\{ \int (1 - \alpha) i_{q,k} * + \int [\eta e_{k+1} + \zeta \int e_{k+1} dt] dt \right\} \tag{16}$$

where J is the inertia moment, n_p is the pole pair of the motor, and k_t is the torque coefficient. Therefore, the following formulas are obtained:

$$\|e_{k+1}\|_\infty = \max_{0 \leq t \leq T} \left| (1 - \alpha) e_k + \alpha \omega_{ref} - \frac{n_p k_t}{J} \int_0^t [\eta e_{k+1} + \zeta \int_0^t e_{k+1} dt] dt \right| \tag{17}$$

The definition of the infinite parametric number and the absolute value inequality leads to:

$$\left| 1 - \frac{n_p k_t}{J} (\eta t + \frac{1}{2} \zeta t^2) \right| \|e_{k+1}\|_\infty \leq |1 - \alpha| \|e_k\|_\infty + \alpha \|\omega_{ref}\|_\infty \tag{18}$$

When $\lim_{k \rightarrow \infty} e_k(t) = 0$, the algorithm converges by considering the convergence condition of the PI-ILC algorithm:

$$\left| \frac{J(1 - \alpha)}{J - n_p k_t \eta T - 0.5 n_p k_t \zeta t^2} \right| < 1 \tag{19}$$

where $t \in [0, T]$, T is the system tracking time.

3. Application of Multi-Parameter Fuzzy-Based Neural Network for Parameter Auto-Tuning

The principle of neural network is to analysis errors based on training and online results, modify weights and thresholds, and iteratively obtain models with the online results as outputs. It consists of input and output layer nodes, as well as one or more hidden layer nodes. The input information must be propagated forward to the hidden layer, and the activated information is passed to each output node after the activation function operation of the unit node to obtain the output results.

Fuzzy neural networks (FNNs) have good self-learning and adaptive abilities with strong robustness that only relies on fuzzy rules [25–29]. They can perform logical reasoning through established fuzzy rules which have good approximation abilities for certain complex nonlinear systems.

The proposed algorithm consists of an ILC algorithm, adaptive STA-SMO algorithm, and FNN algorithm. FNNs can generate fuzzy rules and adjust affiliation functions through strong self-learning and adaptive training. The control system transfers the speed deviation $e(t)$ and the deviation rate $ec(t)$ to the FNN, which can adjust the ILC parameters α , η , and

ζ and the STA-SMO parameters σ_1 and σ_2 to achieve better speed control performance after the fuzzification, fuzzy inference, and anti-fuzzification of the output.

The structure block diagram of FNN is shown as Figure 5. The four layers are input, fuzzification, fuzzy inference, and output layers in order. The calculation formula for input layer is shown as follows:

$$\begin{cases} x_1 = e(t) \\ x_2 = ec(t) \\ o_1(i) = [x_1, x_2] \end{cases} \quad (20)$$

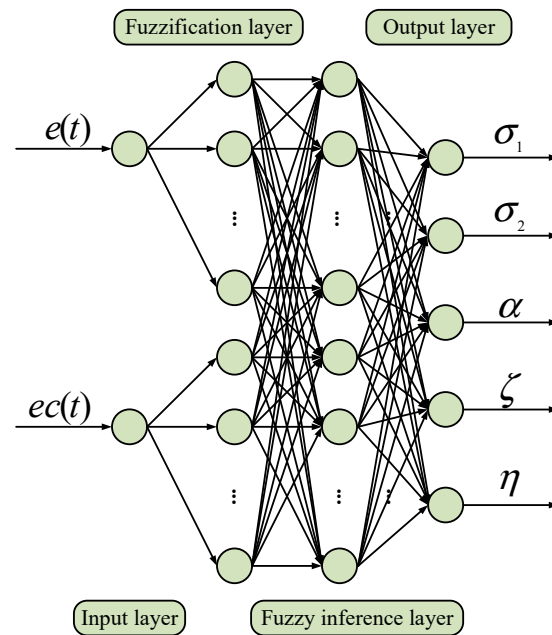


Figure 5. Structure block diagram of FNN.

The fuzzification layer considers a Gaussian membership function as the analysis method, which is shown as:

$$\begin{cases} o_2(i, j) = \exp\left(-[o_1(i) - c_{ij}]^2 / (b_{ij})^2\right) \\ i = 1, 2; j = 1, 2, \dots, n \end{cases} \quad (21)$$

in which c_{ij} is the central value of membership function; b_{ij} represents the width of function curve; and n is the number of fuzzy subsets.

The calculation formula for the fuzzy inference layer is shown as:

$$\begin{cases} o_3(i) = o_2(1, k) \times o_2(2, k) \\ k_1 = 1, 2, \dots, 5; k_2 = 1, 2, \dots, 5 \\ i = 1, 2, \dots, 25 \end{cases} \quad (22)$$

The calculation formula for the output layer is shown as follows:

$$\begin{cases} o_4(i) = \sum_{j=1}^{25} o_3(j) \times \omega_{ij} \\ i = 1, 2, 3 \end{cases} \quad (23)$$

in which ω_{ij} is the weight coefficient.

The ILC and STA-SMO control parameters output by the output layer are shown as:

$$o_4(1) = \sigma_1, o_4(2) = \sigma_2, o_4(3) = \eta, o_4(4) = \zeta, o_4(5) = \alpha \quad (24)$$

The parameters to be learned by the FNN are the affiliation function center value c_{ij} , the width value b_{ij} , and the weight value ω_{ij} , and the objective function is shown as follows:

$$E(k) = \frac{1}{2} [r(k) - y(k)]^2 \tag{25}$$

in the formula, $r(k)$, $y(k)$, and $r(k) - y(k)$ are the expected output, actual output of each network learning, and the control error.

The learning algorithm for the centroid, width, and weight of the affiliation function is shown as:

$$\begin{cases} c_{ij}(k+1) = c_{ij}(k) + \lambda \frac{\partial E(k)}{\partial c_{ij}(k)} + \mu \Delta c_{ij}(k) \\ b_{ij}(k+1) = b_{ij}(k) + \lambda \frac{\partial E(k)}{\partial b_{ij}(k)} + \mu \Delta b_{ij}(k) \\ \omega_{ij}(k+1) = \omega_{ij}(k) + \lambda \frac{\partial E(k)}{\partial \omega_{ij}(k)} + \mu \Delta \omega_{ij}(k) \end{cases} \tag{26}$$

where k is the iterative steps of network, λ represents the learning rate, and μ represents the inertia coefficient.

The block diagram of FNN and control system is presented in Figure 6:

- (1) Determine neural network framework through number of layers and nodes in each network layer and select initial weights, learning rate, and momentum factor.
- (2) Calculate the objective function obtained by running k times.
- (3) Calculate the input and output values of each network layer.
- (4) Calculate the output of the self-disturbance rejection controller.
- (5) Perform backpropagation calculations to correct the weights of output and hidden layers.
- (6) If successful, end iteration; if not, return to step (2).

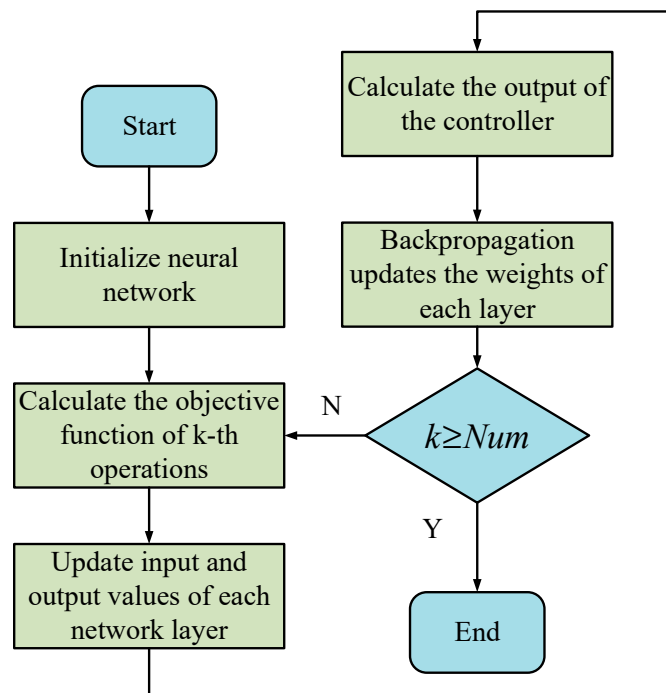


Figure 6. Block diagram of fuzzy neural network ILC control system.

4. Simulation Results and Discussions

The simulation model in this paper is based on MATLAB R2017b/Simulink environment. The structure block diagram of sensorless control model for RDT motor is shown in Figure 7. The main parameters of the RDT motor in simulation are summarized in Table 1.

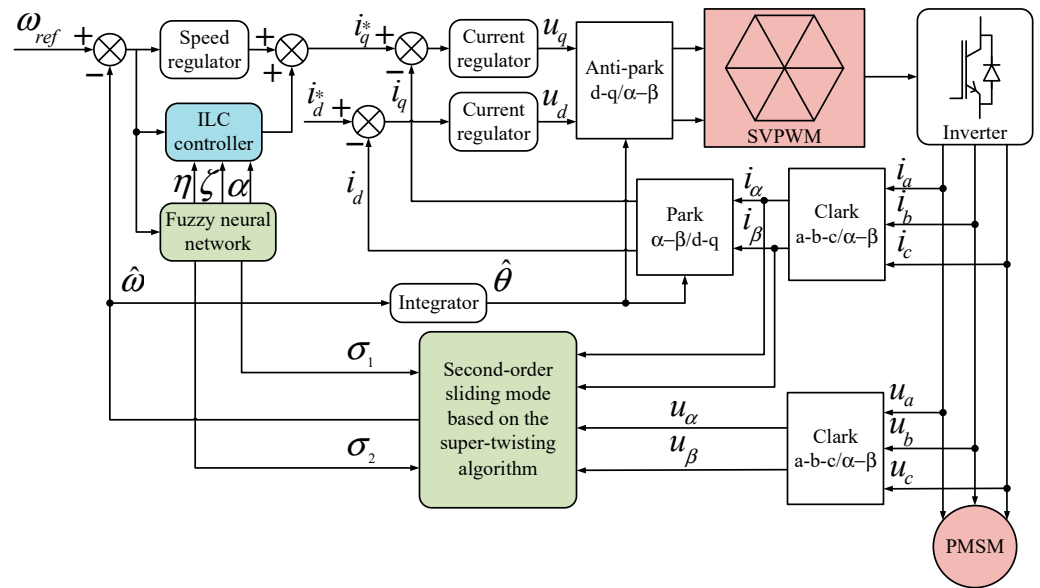


Figure 7. Structure block diagram of sensorless control for RDT motor.

Table 1. Main parameters of RDT motor.

Parameters	Value
Number of motor pole pairs (p)	10
Rotor flux (ψ_f)	0.0078 Wb
Rated voltage (U)	48 V
Inertia moment (J)	0.00106 kg·m ²
Rated power (P _e)	0.7 kW
Resistance (R)	0.061 Ω
Inductance (L)	0.12 mH

To verify the system control performance based on the proposed algorithm, comparisons between conventional PI-STA and modified ILC-STA have been carried out through simulations. The motor starts with the initial given speed of 1200 r/min, the load torque changes to 1.5 N·m at 0.4 s, the given speed changes to 800 r/min at 0.6 s, and the load torque changes back to 0 at 0.9 s.

The simulation results of the RDT motor using conventional PI-STA algorithm are shown in Figure 8. From top to bottom, the estimated speed and actual speed, the speed error, the given torque and electromagnetic torque, the estimated and actual position, and the position error and the three-phase stator currents are presented. It can be seen that the speed error is about −3 and 22 r/min under the 1200 r/min given speed and about −1 and 12 r/min under the 800 r/min given speed. The torque errors are about −1.2 and 1.1 Nm, −1.1 and 1.2 Nm, −1.3 and 1.2 Nm, and −0.9 and 0.8 Nm, respectively. The position error of the RDT motor is about 0.7 rad.

The simulation results of the RDT motor using modified ILC-STA are shown in Figure 9. It can be seen that the speed error is about −2 and 11 r/min under the 1200 r/min given speed and about −1 and 7 r/min under the 800 r/min given speed. The torque errors are about −0.4 and 0.4 Nm, −0.6 and 0.6 Nm, −0.5 and 0.5 Nm, and −0.5 and 0.5 Nm, respectively. The estimated position error of the RDT motor is about 0.7 rad.

From the simulation results, it can be seen that compared to the conventional PI-STA, the modified ILC-STA produces smaller speed and torque errors. The estimated position error is almost the same. The RDT motor speed, torque, and stator currents results display less chattering. This proves that the modified algorithm obviously maintains better control performance. Table 2 shows the performance comparison of different control algorithms.

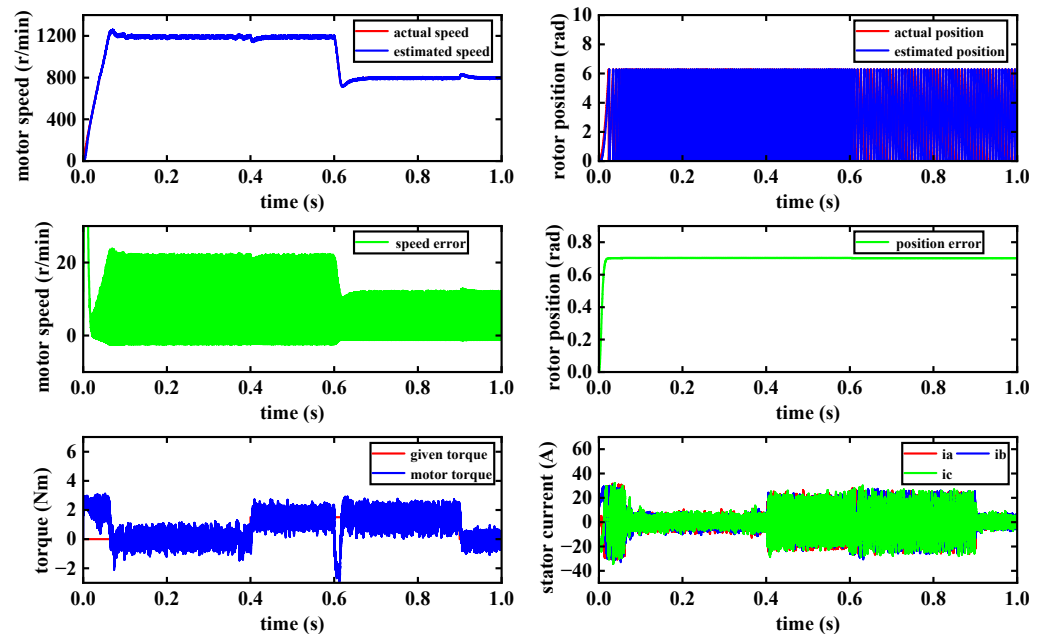


Figure 8. Simulation results using conventional PI-STA.

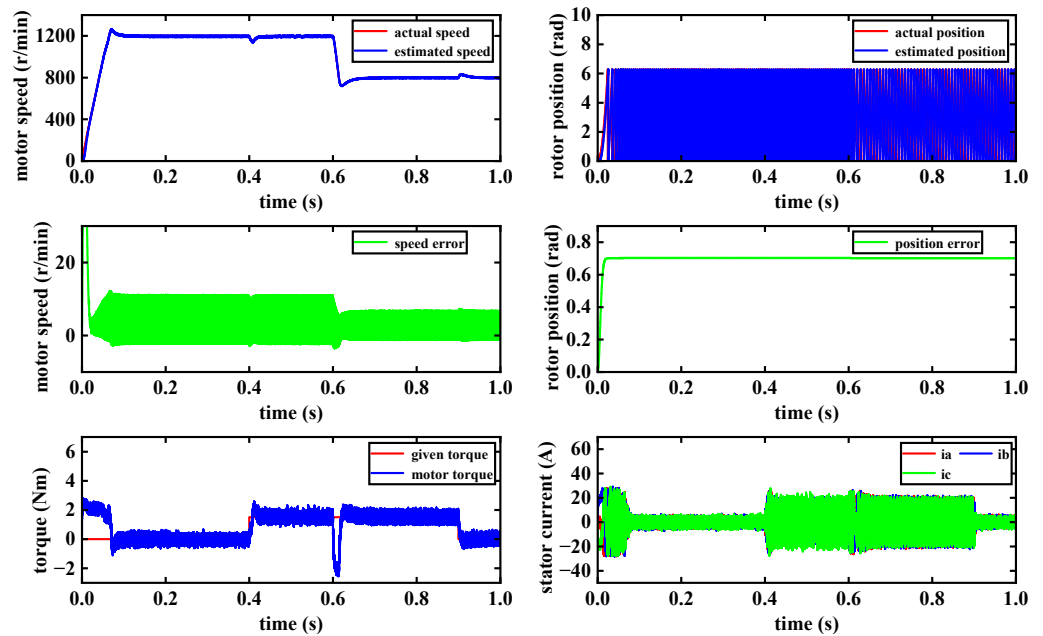


Figure 9. Simulation results using modified ILC-STA.

Table 2. Simulation performance comparison of different control algorithms.

Control Algorithm	Speed Error Ripple (r/min)	Torque Ripple (Nm)	Maximum Speed Error (r/min)
Conventional PI-STA	25/13	2.3/2.3/2.5/1.7	22/12
Modified ILC-STA	13/8	0.8/1.2/1/1	11/7

5. Experimental Results and Discussions

In order to verify the performance of the RDT motor sensorless control algorithm, a TMS320F28335 DSP-based experimental setup was built, as shown in Figure 10. The experimental setup consists of a magnetic powder brake, a torque sensor, and a test RDT motor, which are fixed together on a T-slotted platform and connected by elastic couplings.

The main parameters of the test RDT motor are the same as that in the simulation. And the experimental results under different conditions are shown in Figures 11–13.

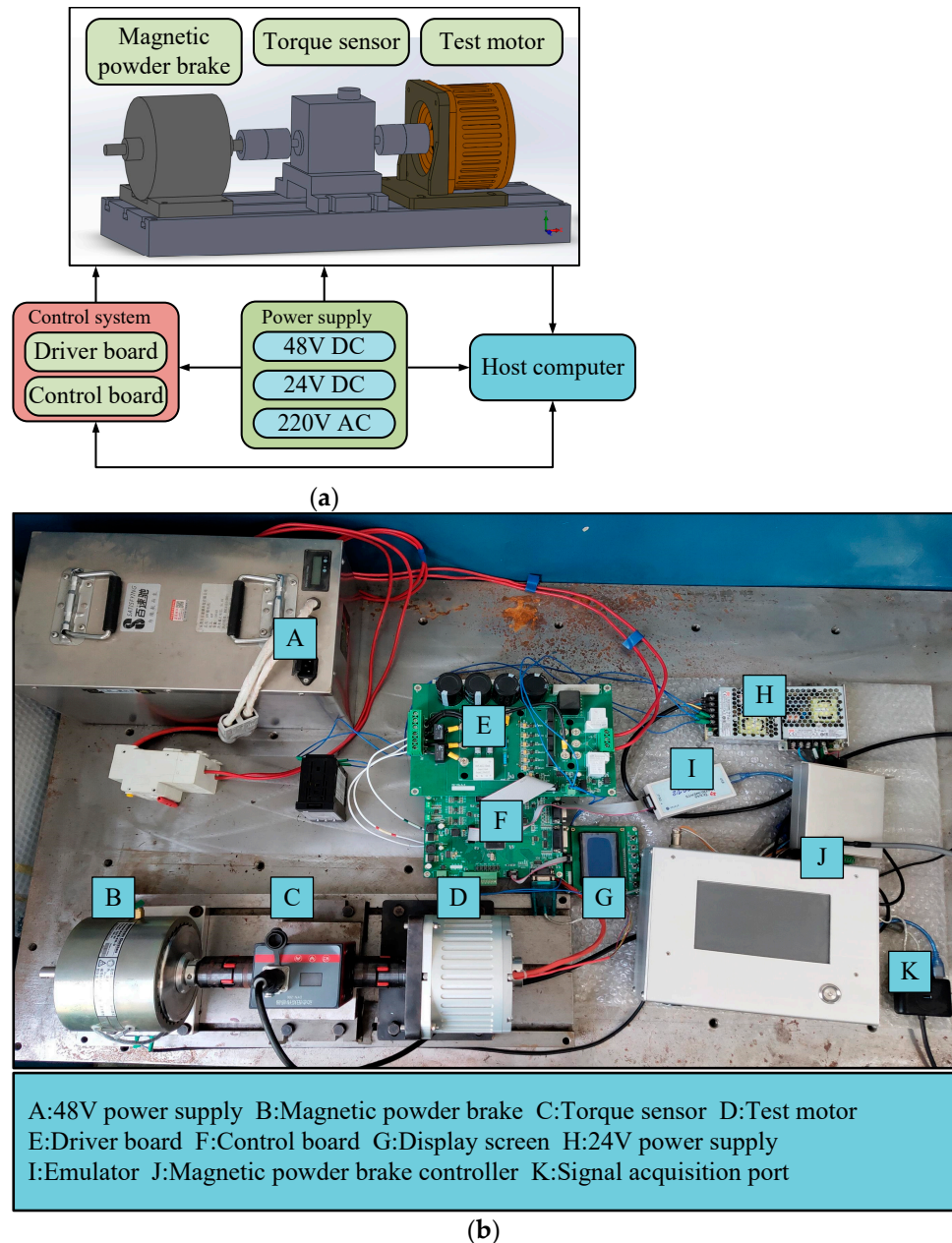


Figure 10. Experimental setup for the RDT motor. (a) Block diagram of experimental setup. (b) Diagram of physical experimental setup.

Condition 1: The tested given speed is set to 1200 r/min with sudden load torque changes from 0 to 1.5 Nm. Figure 11 shows the experimental results comparison between the conventional PI-STA and the modified ILC-STA in each case of step change in load torque. From top to bottom, the estimated speed and actual speed, the speed error, the given torque and electromagnetic torque, the estimated and actual position, the position error, and the three-phase stator currents are plotted. It can be observed that the stable error of the modified algorithm is smaller than that of the conventional algorithm. The motor speed estimation error ripple is about -2 and 22 r/min, respectively. The motor speed error ripple is about 24 r/min, and the electromagnetic torque ripples are about 2.2 Nm and 3 Nm, respectively. The rotor position error between the estimate and actual value of RDT motor is about 0.7 rad. When the modified ILC-STA is used, the motor speed estimation

errors are about -2 and 11 r/min, respectively. The motor speed error ripple is about 13 r/min, and the electromagnetic torque ripples are about 0.9 Nm and 1 Nm, respectively. The rotor position error between the estimate and actual value of RDT motor is also about 0.7 rad. From Figure 11, it can be seen that the motor speed and electromagnetic torque waveforms are more stable, and the ripple is smaller than when using the conventional algorithm. The RDT motor speed error ripple decreases by 46% and the torque ripple decreases by 59% and 67% , respectively. The maximum speed error decreases by 11 r/min.

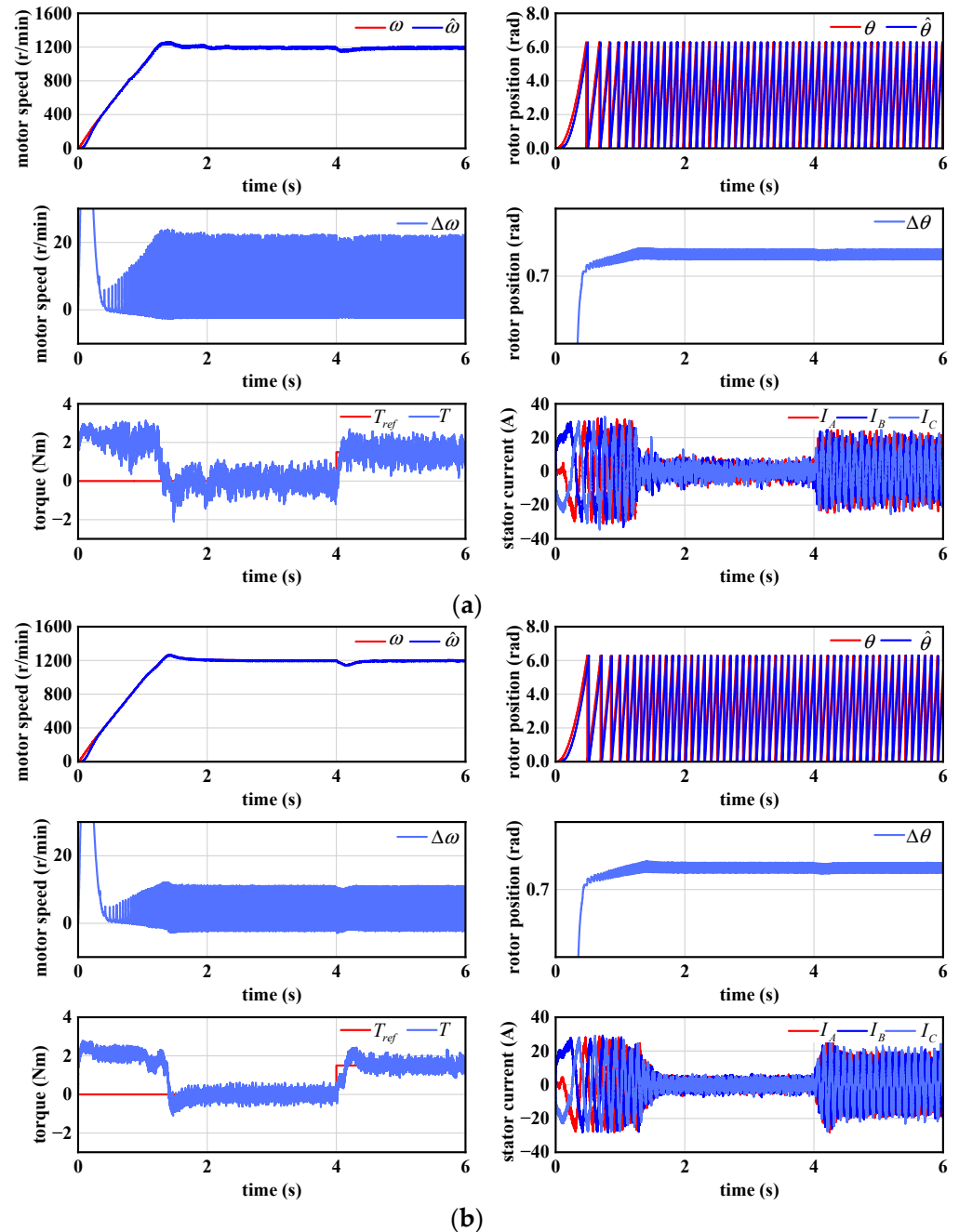


Figure 11. Experimental results under a step change of the load torque condition. (a) Conventional PI-STA. (b) Modified ILC-STA.

Condition 2: The tested given speed decreases from 1200 r/min to 800 r/min, with a continuous load torque of 1.5 Nm. Figure 12 shows the experimental results comparison between conventional PI-STA and modified ILC-STA in case of a step change in given speed. It is obvious that the stable error of the modified algorithm is smaller than that of

the conventional algorithm. The motor speed estimation error ripples are about -1 and 12 r/min, respectively. The motor speed error ripple is about 13 r/min, and the electromagnetic torque ripple is about 2.5 Nm. When the modified ILC-STA algorithm is used, the motor speed estimation errors are about -1 and 7 r/min, respectively. The motor speed error ripple is about 8 r/min, and the electromagnetic torque ripple is about 1 Nm. From Figure 12, it can be seen that the motor actual speed and electromagnetic torque waveforms are more stable and the ripple is smaller than when using conventional algorithm. The RDT motor speed error ripple and torque ripple decrease by 38% and 60% , respectively. The maximum speed error decreases by 5 r/min.

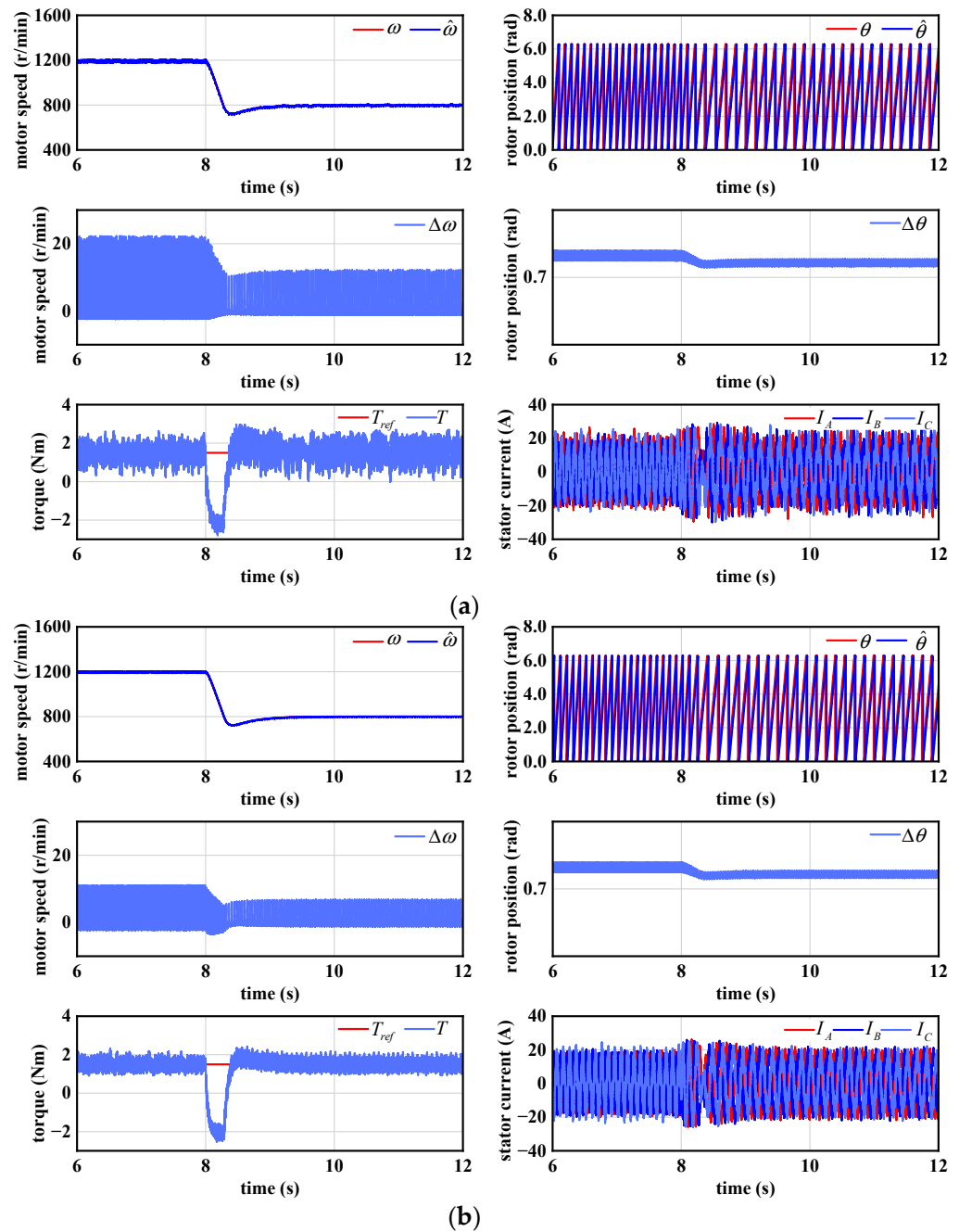


Figure 12. Experimental results under a step change of a given speed condition. (a) Conventional PI-STA. (b) Modified ILC-STA.

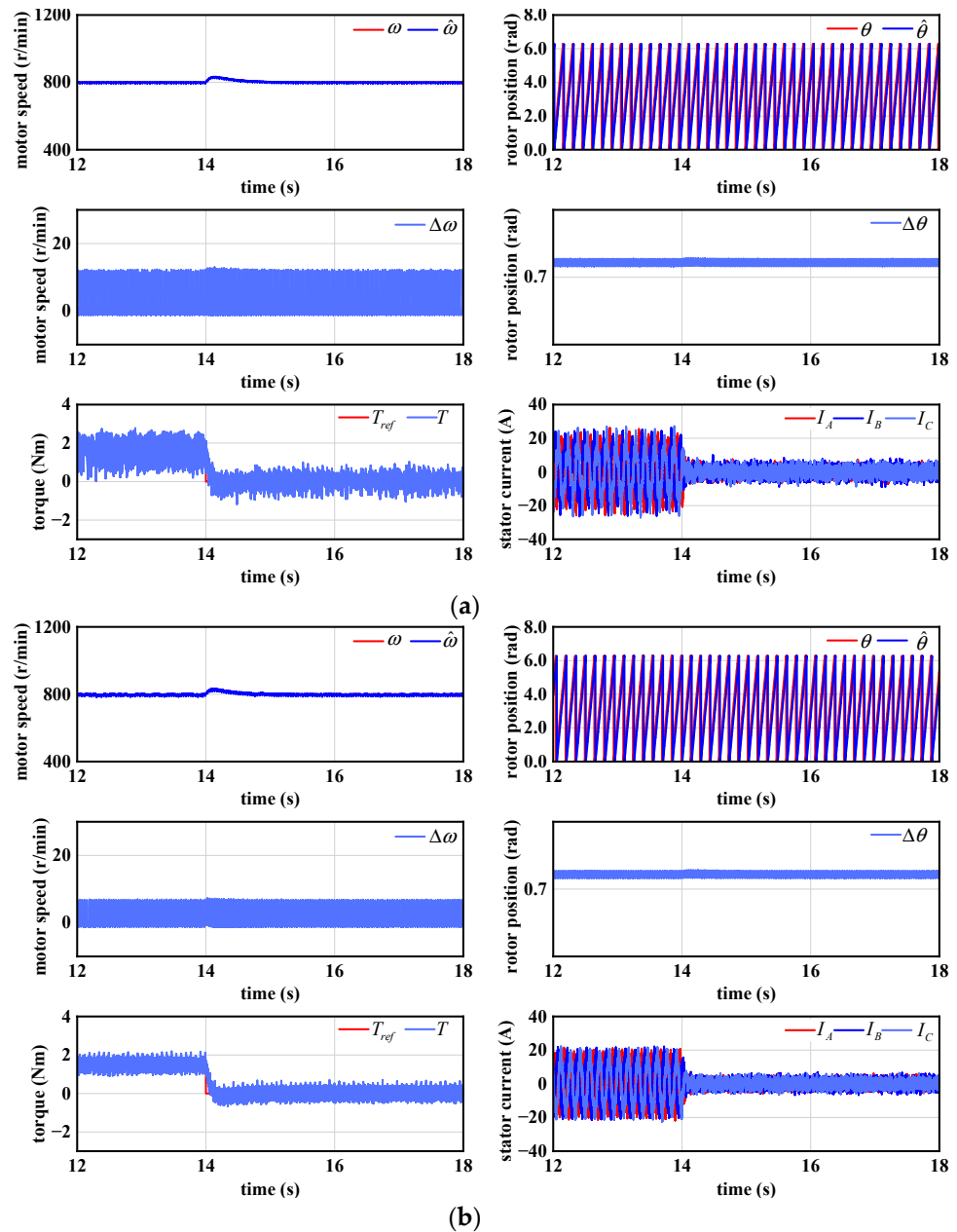


Figure 13. Experimental results under a step change of the load torque condition. (a) Conventional PI-STA. (b) Modified ILC-STA.

Condition 3: The tested given speed is set as the speed of 800 r/min with sudden load torque changes from 1.5 Nm to 0. Figure 13 shows the experimental results comparison between conventional PI-STA and modified ILC-STA in the case of step change in load torque. Similarly to the previous conditions, it is obvious that the stable error of the modified algorithm is smaller than that of the conventional algorithm. The motor speed estimation error ripples are about -1 and 12 r/min, respectively. The motor speed error ripple is about 13 r/min, and the electromagnetic torque ripple is about 1.7 Nm. When the modified ILC-STA algorithm is used, the motor speed estimation errors are about -1 and 7 r/min, respectively. The motor speed error ripple is about 8 r/min, and the electromagnetic torque ripple is about 1 Nm. Similarly to the previous conditions, it is obvious that the motor speed and electromagnetic torque waveform are more stable and the ripple is smaller than when using conventional method. The speed error ripple and

torque ripple decrease by 38% and 41%, respectively. The maximum speed error decreases by 5 r/min.

Similarly to the simulation results, it can be seen from the experimental results that compared to the conventional PI-STA, the modified ILC-STA produces lower speed errors and smaller electromagnetic torque errors. The motor speed, electromagnetic torque, and stator currents results also have less chattering. Table 3 summarizes the performance comparison of the different control algorithms.

Table 3. Experimental performance comparison of different control algorithms.

Control Algorithm		Speed Error Ripple (r/min)	Torque Ripple (Nm)	Maximum Speed Error (r/min)
Conventional PI-STA	Condition 1	24	2.2/3	22
	Condition 2	13	2.5	12
	Condition 3	13	1.7	12
Modified ILC-STA	Condition 1	13	0.9/1	11
	Condition 2	8	1	7
	Condition 3	8	1	7

6. Conclusions

In this paper, a RDT motor position-sensorless control algorithm that uses an adaptive second-order SMO based on STA is presented to reduce system chattering, and a closed-loop PI-ILC algorithm with the forgetting factor is used to suppress torque vibration. In addition, FNN training is used to optimize the ILC and STA-SMO parameters. The simulation and experimental analysis have been used to verify the proposed algorithm. The presented RDT sensorless control algorithm can be used to reduce the chattering generated in the RDT motor speed and torque ripple with improved speed tracking accuracy. The accuracy and complexity have been balanced and can be used to explore future research.

Our future work will apply the presented RDT sensorless control algorithm to a real ship, which will greatly contribute to the realization of smart and low carbon emission-oriented maritime traffic control technology.

Author Contributions: Conceptualization, Z.Y. and H.B.; methodology, Z.Y. and H.B.; software, Z.Y.; validation, Z.Y.; formal analysis, Z.Y.; investigation, Z.Y.; resources, Z.Y.; data curation, Z.Y.; writing—original draft preparation, Z.Y.; writing—review and editing, Z.Y., X.Y., W.O., H.B. and J.X.; visualization, Z.Y.; supervision, X.Y., W.O., H.B. and J.X.; project administration, X.Y., W.O. and H.B.; funding acquisition, X.Y., W.O. and H.B. All authors have read and agreed to the published version of the manuscript.

Funding: This research was partly funded by the National Key Research and Development Project, grant number 2022YFB4300802, and partly funded by the European Union’s Horizon 2020 Research and Innovation Programme RISE, under grant agreement no. 823759, REMESH.

Institutional Review Board Statement: Not applicable.

Informed Consent Statement: Not applicable.

Data Availability Statement: Data are contained within the article.

Conflicts of Interest: The authors declare no conflicts of interest.

References

1. Yan, X.; Liang, X.; Ouyang, W.; Liu, Z.; Liu, B.; Lan, J. A review of progress and applications of ship shaft-less rim-driven thrusters. *Ocean Eng.* **2017**, *144*, 142–156. [\[CrossRef\]](#)
2. Yang, Z.; Yan, X.; Ouyang, W.; Bai, H. A Review of Electric Motor and Control Technology for Rim-Driven Thruster. *Trans. China Electrotech. Soc.* **2022**, *37*, 2949–2960. [\[CrossRef\]](#)
3. Wang, D.; Jin, S.B.; Wei, Y.S. Review on The Integrated Electric Propulsion System Configuration and its Applications. *Proc. CSEE* **2020**, *40*, 3654–3663.

4. Wang, G.L.; Valla, M.; Solsona, J. Position Sensorless Permanent Magnet Synchronous Machine Drives—A Review. *IEEE Trans. Ind. Electron.* **2020**, *67*, 5830–5842. [[CrossRef](#)]
5. Yang, H.; Yang, R.; Hu, W.; Huang, Z. FPGA-Based Sensorless Speed Control of PMSM Using Enhanced Performance Controller Based on the Reduced-Order EKF. *IEEE J. Emerg. Sel. Top. Power Electron.* **2021**, *9*, 289–301. [[CrossRef](#)]
6. Wang, G.; Hao, X.; Zhao, N.; Zhang, G.; Xu, D. Current Sensor Fault-Tolerant Control Strategy for Encoderless PMSM Drives Based on Single Sliding Mode Observer. *IEEE Trans. Transp. Electrification.* **2020**, *6*, 679–689. [[CrossRef](#)]
7. Bernard, P.; Praly, L. Estimation of Position and Resistance of a Sensorless PMSM: A Nonlinear Luenberger Approach for a Nonobservable System. *IEEE Trans. Autom. Control.* **2021**, *66*, 481–496. [[CrossRef](#)]
8. Abo Khalil, A.G.; Eltamaly, A.M.; Alsaoud, M.S.; Sayed, K.; Alghamdi, A.S. Sensorless control for PMSM using model reference adaptive system. *Int. Trans. Electr. Energy Syst.* **2021**, *31*, e12733. [[CrossRef](#)]
9. Wu, L.; Liu, J.; Vazquez, S.; Mazumder, S.K. Sliding Mode Control in Power Converters and Drives: A Review. *IEEE-CAA J. Autom. Sin.* **2022**, *9*, 392–406. [[CrossRef](#)]
10. Ren, N.N.; Fan, L.; Zhang, Z. Sensorless PMSM Control with Sliding Mode Observer Based on Sigmoid Function. *J. Electr. Eng. Technol.* **2021**, *16*, 933–939. [[CrossRef](#)]
11. Kang, W.; Li, H. Improved sliding mode observer based sensorless control for PMSM. *IEICE Electron. Express* **2017**, *14*, 20170934. [[CrossRef](#)]
12. Ye, S.C.; Yao, X.X. An Enhanced SMO-Based Permanent-Magnet Synchronous Machine Sensorless Drive Scheme with Current Measurement Error Compensation. *IEEE J. Emerg. Sel. Top. Power Electron.* **2021**, *9*, 4407–4419. [[CrossRef](#)]
13. Yang, Z.B.; Ding, Q.F.; Sun, X.D.; Lu, C.L.; Zhu, H.M. Speed Sensorless Control of a Bearingless Induction Motor Based on Sliding Mode Observer and Phase-Locked Loop. *ISA Trans.* **2022**, *123*, 346–356. [[CrossRef](#)] [[PubMed](#)]
14. Gong, C.; Hu, Y.H.; Gao, J.Q.; Wang, Y.G.; Yan, L.M. An Improved Delay-Suppressed Sliding-Mode Observer for Sensorless Vector-Controlled PMSM. *IEEE Trans. Ind. Electron.* **2020**, *67*, 5913–5923. [[CrossRef](#)]
15. Liang, D.L.; Li, J.; Qu, R.H. Sensorless Control of Permanent Magnet Synchronous Machine Based on Second-order Sliding-mode Observer with Online Resistance Estimation. *IEEE Trans. Ind. Appl.* **2017**, *53*, 3672–3682. [[CrossRef](#)]
16. Liang, D.L.; Li, J.; Qu, R.H. Adaptive Second-order Sliding-mode Observer for PMSM Sensorless Control Considering VSI Nonlinearity. *IEEE Trans. Power Electron.* **2017**, *33*, 8994–9004. [[CrossRef](#)]
17. Nakao, N.; Akatsu, K. Suppressing pulsating torques: Torque ripple control for synchronous motors. *IEEE Ind. Appl. Mag.* **2014**, *20*, 33–44. [[CrossRef](#)]
18. Chen, Z.F.; Li, Z.X.; Ma, H.Z. A harmonic current injection method for electromagnetic torque ripple suppression in permanent-magnet synchronous machines. *Int. J. Appl. Electromagn. Mech.* **2017**, *53*, 327–336. [[CrossRef](#)]
19. Zhang, H.Y.; Xu, H.P.; Fang, C. Torque ripple suppression method of direct drive permanent magnet synchronous motor based on proportional-integral and quasi resonant controller. *Trans. China Electrotech. Soc.* **2017**, *32*, 41–51.
20. Liu, J.; Li, H.; Deng, Y. Torque ripple minimization of PMSM based on robust ILC via adaptive sliding mode control. *IEEE Trans. Power Electron.* **2018**, *33*, 3655–3671. [[CrossRef](#)]
21. Dang, X.J.; Miao, M.Y.; Jiang, H. Torque ripple suppression for switched reluctance motors based on current self-adaptive control. *J. Vib. Shock* **2018**, *37*, 66–71.
22. Levant, A. Sliding order and sliding accuracy in sliding mode control. *Int. J. Control* **1993**, *58*, 1247–1263. [[CrossRef](#)]
23. Moreno, J.A.; Osorio, M. Strict lyapunov functions for the super-twisting algorithm. *IEEE Trans. Autom. Control* **2012**, *57*, 1035–1040. [[CrossRef](#)]
24. Moreno, J.A.; Osorio, M. A lyapunov approach to second-order sliding mode controllers and observers. In Proceedings of the 47th IEEE Conference on Decision and Control, Cancun, Mexico, 9–11 December 2008.
25. Chen, X.; Liu, S.; Liu, R.W.; Wu, H.; Han, B.; Zhao, J. Quantifying Arctic oil spilling event risk by integrating an analytic network process and a fuzzy comprehensive evaluation model. *Ocean Coast Manag.* **2022**, *228*, 106326. [[CrossRef](#)]
26. Damien, F.; Ngac, K.N.; Patric, W. A self-learning solution for torque ripple reduction for non-sinusoidal permanent magnet motor drives based on artificial neural networks. *IEEE Trans. Ind. Electron.* **2014**, *61*, 655–666.
27. Wu, B.F.; Lin, C.H. Adaptive neural predictive control for permanent magnet synchronous motor systems with long delay time. *IEEE Access* **2019**, *7*, 108061–108069. [[CrossRef](#)]
28. Yang, S.Q.; Chen, C. Application of fuzzy neural network PID algorithm in oil pump control. In Proceedings of the 2019 International Conference on Computer Network, Electronic and Automation (ICCNEA), Xi'an, China, 27–29 September 2019.
29. Chen, X.; Wang, M.; Ling, J.; Wu, H.; Wu, B.; Li, C. Ship imaging trajectory extraction via an aggregated you only look once (YOLO) model. *Eng. Appl. Artif. Intell.* **2024**, *130*, 107742. [[CrossRef](#)]

Disclaimer/Publisher's Note: The statements, opinions and data contained in all publications are solely those of the individual author(s) and contributor(s) and not of MDPI and/or the editor(s). MDPI and/or the editor(s) disclaim responsibility for any injury to people or property resulting from any ideas, methods, instructions or products referred to in the content.